INTERNATIONAL JOURNAL OF CIRCUIT THEORY AND APPLICATIONS
Int. J. Circ. Theor. Appl. 2013; **41**:653–667
Published online 20 July 2012 in Wiley Online Library (wileyonlinelibrary.com). DOI: 10.1002/cta.1829

Design and Implementation of a Modular Biomimetic Infochemical Communication System

Z. Rácz[1,*,†], M. Cole[1], J.W. Gardner[1], M.F. Chowdhury[1], W.P. Bula[2], J.G.E. Gardeniers[2], S. Karout[3], A. Capurro[3] and T.C. Pearce[3]

[1]*Microsensors and Bioelectronics Laboratory, University of Warwick, Coventry, UK*
[2]*MESA + Institute for Nanotechnology, University of Twente, Enschede, The Netherlands*
[3]*Centre for Bioengineering, University of Leicester, Leicester, UK*

SUMMARY

We describe here the design and implementation of a novel biomimetic infochemical communication system that employs airborne molecules alone to communicate over space and time. The system involves the design and fabrication of a microsystem capable of producing and releasing a precise mix of biosynthetic compounds and a sensor system capable of detecting and decoding the ratiometrically encoded chemical information.

The research inspired by biology has been based upon the biosynthetic pathways of infochemical production and information processing within the insect world. In this novel approach, the functional equivalents of the nanoscale biological machinery are implemented by combining the latest advances and convergence of expertise in the fields of biochemistry, molecular biology, neuroscience, micro- and nanofabrication, materials science, and smart sensor and microcircuit design. The biomimetic system comprises a micromachined bio-reactor mimicking the sex gland of the female insect that releases a blend of pheromones in precisely controlled ratios, together with a cell-based biosensor system, mimicking the antennae of the male insect. The signals from the biosensors are classified and ratios decoded using a field-programmable gate array implementation of a neuromorphic model of the antenna lobe of the insect.

We believe that this novel, smart infochemical communication system, inspired by the insect's behavior, could eventually be implemented in VLSI technology at low cost and low power with possible application in the fields of automatic identification and data capturing, product labeling, search and rescue, environmental monitoring, and pest control.

Received 4 July 2011; Revised 27 February 2012; Accepted 24 June 2012

KEY WORDS: biomimetic; SAWl; biosensor; olfactory receptor; biosynthesisl; neuromorphic network

1. INTRODUCTION

Information exchange utilizing chemicals is a ubiquitous mode of communication in nature. Living organisms rely on chemical communication for a range of diverse behaviors such as locating food sources, organizing communities, avoiding dangers, and attracting conspecific mates [1]. Insects, in particular, have extremely sophisticated low-power chemical signaling and processing systems. Infochemical signals are produced by generating a spatially and temporally defined combination of chemical compounds that are often synthesized *de novo* within the insect.

This extremely efficient form of communication employed by insects can serve as a blueprint for building a new class of technologies for molecular labeling, information transmission, and cellular communication.

*Correspondence to: Zoltan Racz, Microsensors and Bioelectronics Laboratory, University of Warwick, *Coventry, UK*.
†E–mail: z.racz@warwick.ac.uk

A moth, *Spodoptera littoralis*, served as the biological inspiration for the development of the technologies described in this paper. This insect is an ideal choice because it uses a precisely controlled blend of infochemicals (i.e. pheromones) that are well-known, and the biosynthesis steps needed to produce them have been well-characterized [2]. The infochemical-mediated behavior in the insect is robustly reproducible, the candidate olfactory receptors (ORs) responsible for infochemical detection have been identified, and the subsequent blend ratio decoding in the insect is becoming understood [3].

In our system, similar to the female moth's pheromone producing and releasing apparatus, a microsystem, termed the *chemoemitter*, is used to generate a precise mixture of predefined volatile compounds in programmable discrete ratios of concentration.

The operation of the detection system, termed *chemoreceiver*, mimics the molecular detection in the receptor/antenna of insects and the neuromorphic signal processing in the antennal lobe (AL) within the mushroom body. The chemoreceiver is designed to be a tuned detector of the emitted volatile chemical mixture that is able to recover the ratiometrically encoded information using complementary ORs, acousto-electric or optical transduction, and a data processing architecture.

As a combined system, this innovative modular arrangement is capable of information transmission using chemicals alone [4] and serves as the foundation of a new technological field for labeling, information transmission, and biochemical interfacing [5] with numerous applications such as automatic identification and data capture, product labeling, search and rescue, air silent communication, medical diagnosis/treatment, and environmental monitoring/control.

2. IMPLEMENTATION OF INFOCHEMICAL COMMUNICATION

2.1. System - overview

The technological implementation of the above described communication system involves the design and fabrication of a microsystem capable of producing and releasing a precise mix of biosynthetic compounds and a sensor system capable of detecting the biosynthetic ligands and decoding ratiometrically encoded information.

To implement both chemical signal generation and reception, we adopted a modular approach - thus engineering each step of the pathway as stand-alone bio-inspired modules which were integrated into a complete system providing a technological solution to infochemical communication. A prototype of the micro- and nanofabricated implementation of the integrated artificial biomimetic infochemical communications system utilizing biosynthetic modules is shown in Figure 1.

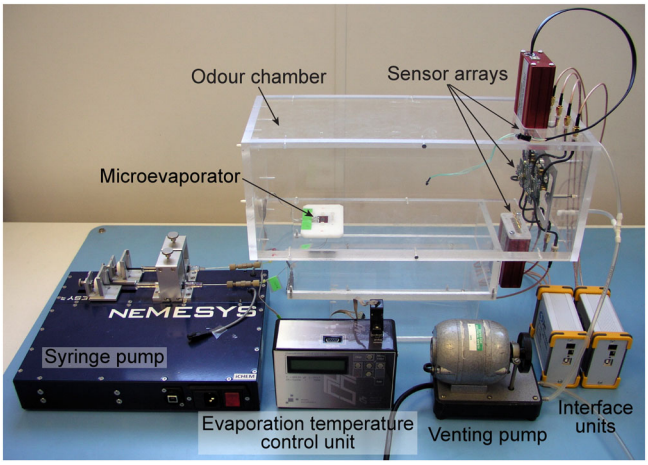

Figure 1. Set Q ⊂ R2 and cones TQ and NQ at points a, b, and c of Q (the cones are shown translated into the corresponding points of Q).

DOI: 10.1002/cta

In the chemoemitter, microreactor modules facilitate the immobilization of key enzymes, whilst preserving catalytic activity, and provide accurate control of the concentration and residence time of the reactants and end-products. Ratiometric information encoding is achieved by precisely controlled dilution and mixing of the compounds to produce the required pheromone blends. The synthesized blends are emitted into the environment by a release apparatus via controlled thermal volatilization from a micromachined evaporator or via atomization by a piezoelectric actuator.

The chemoreceiver design utilizes surface acoustic wave (SAW) sensors in dual configuration where one side of the device pair is functionalized while the other side serves as the reference. This differential structure provides reduced noise and better signal stability by compensating for environmental effects and common mode variations. The modular design of the chemoreceiver facilitates the use of different sensor types, for example, polymer-coated SAW arrays for infochemical detection (as shown in Figure 1) or shear-horizontal SAW sensors coated with functionalized cells for biological sensing. The biological sensing module is based on the dual bio-SAW concept [6] and comprises SAW devices coated with OR expressing cells, an acousto-electric resonator circuitry, and a subsequent neuromorphic processing architecture. Pheromone signaling is detected by measuring the variation in the sensor characteristics induced by ligand binding-related changes in the insect cells. The differential output signals are processed to achieve ratio recovery and blend recognition using a biophysically constrained neuromorphic model mimicking the ratiometric processing in the AL of a moth.

2.2. *System – detailed description*

2.2.1. Chemoemitter. Volatile compounds can be released into the environment by several means such as nebulization, acoustic atomization, or thermal evaporation. Thermal evaporation is the most suitable technique to generate precise pheromone evaporation patterns with a broad range of mass fluxes. Moreover, the possibility of controlling the evaporation rates by controlling the temperature and the flow rate of pheromone precursors allows us to design a device compatible with a continuous-flow regime of pheromone production [7].

2.2.1.1. Microevaporator. The key component of the chemoemitter, described here, is a micromachined microevaporator capable of transforming liquid eluents from biological and chemical microreactors into precise ratios of vapor concentration of volatile sex pheromones [8]. Below we describe the design and parameters of the miniaturized evaporator and the peripheral control circuitry.

The microevaporator consists of a silicon membrane (5 mm × 5 mm × 40 μm) perforated with 37,636 micromachined vias (i.e. orifices). Rectangular microfluidic channels deliver the liquid mixture of predefined volatile compounds from two inlets to the reservoir (0.375 μl) located under the membrane. The liquid passes through the orifices of the membrane and evaporates from the small droplets that are formed on the outlet of every orifice. An optical image of the fabricated microevaporator is shown in Figure 2(A) and its cross-sectional schematic diagram in Figure 2(B). The low volume of the device and its reduced dead volume enable fast response times for ratiometric encoding.

2.2.1.2. Digital control module. The membrane of the silicon-glass evaporator was formed on the top side of the silicon wafer by anisotropic etching in KOH solution. On the back side, via-holes through

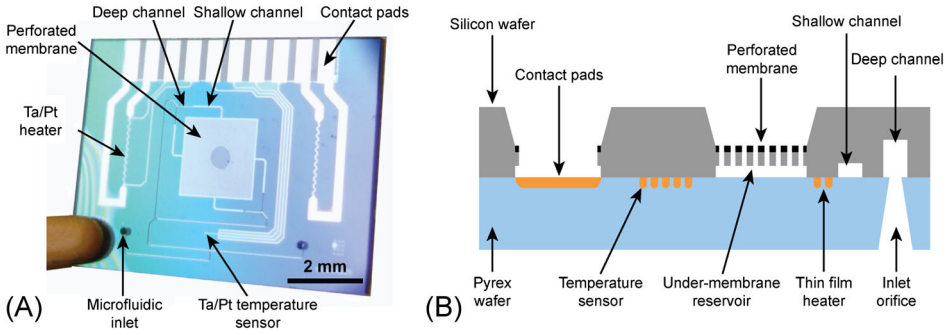

Figure 2. Set K2 = [_1, 1]2 and cones TK2, NK2 at points a, b, and c of K2.

DOI: 10.1002/cta

the membrane were etched together with deep channels (100 μm) by deep reactive ion etching using a mask of photoresist and silicon-rich nitride. The shallow channels and under-membrane cavity were etched to 15 μm with the same process. The silicon wafer was anodically bonded to the Pyrex glass containing the powder-blasted via-holes and the semi-buried tantalum (10 nm) and platinum (200 nm) metallization layers of the heaters and the temperature sensor.

Two thin-film platinum heaters and a four-wire resistive temperature sensor are integrated in the evaporator and work in a proportional-integral-derivative (PID) loop in order to stabilize the temperature within a variation of 30 mK. Integrated heaters dissipate up to 8 W of energy capable of elevating the membrane temperature up to 250 °C.

An autonomous controller was designed and assembled to provide the desired temperature stabilization and response times. The controller consists of a digital board in which the PID loop is implemented by high-level programming language code in an ATMEGA128-16AI microcontroller (AVR-MT-128 development board, OLIMEX Ltd., Bulgaria) and an analog board that powers the heaters and interfaces the temperature sensor with the voltage range of the 10-bit ADC and the 5-V logic of the microcontroller (Figure 3).

The temperature set-point, parameters of the PID regulation loop and PWM, the ADC resolution, RS232C and USB data link speed, and semi-automatic sensor calibration procedure are controlled and stored in the non-volatile memory of the microcontroller. The software-implemented oversampling technique enhanced the resolution of ADC converter to 14 bit which increases the accuracy of temperature stabilization. Serial communication with a monitoring personal computer (PC) is established via an RS232C or a USB interface. The embedded web server connected to the digital board enables remote control of the device.

2.2.1.3. Analogue control module. The resistance of the four-wire Pt temperature sensor is measured using a constant-current technique. A current is supplied to the resistance from the adjustable current source comprising a low-power operational amplifier (TL074) and a voltage reference (LM285-2.5). The resulting differential signal is amplified by a high-impedance instrumentation amplifier (INA129). The subtraction of the reference voltage (LM317) from the signal by the differential amplifier (INA105) followed by further amplification (TL074) conditions the signal to match the 0–5 V input range of the analog-to-digital converter of the microcontroller for the temperature range of 10 to

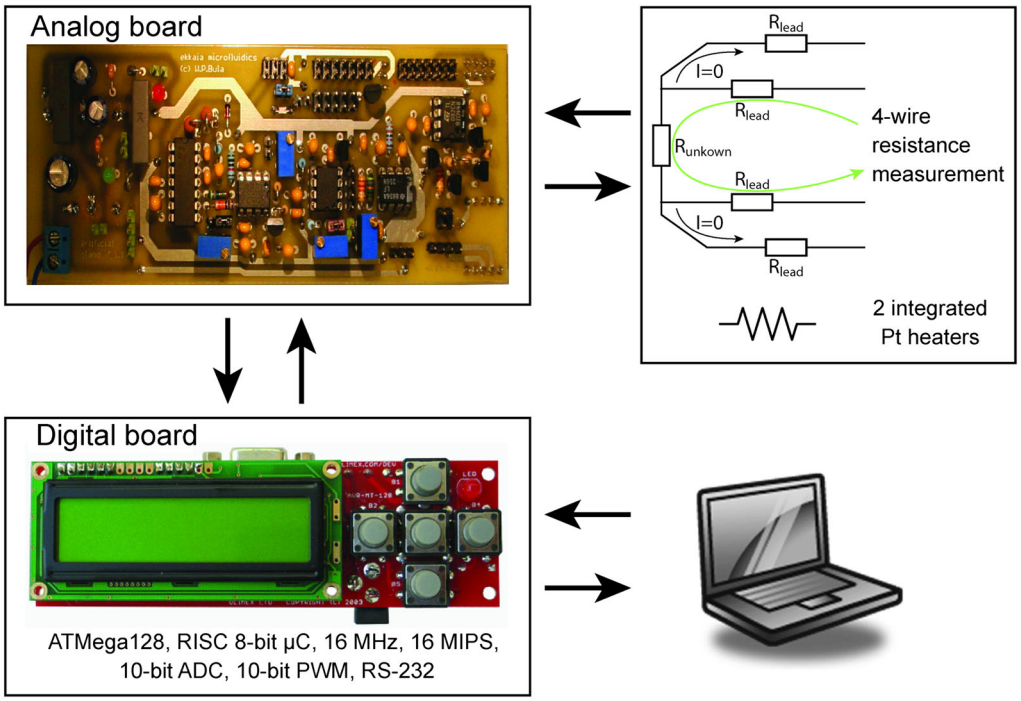

Figure 3. Hard-limiter nonlinearity in the FRCNN model.

DOI: 10.1002/cta

150 °C. Finally, the signal is fed to the digital board through a first-order low-pass filter ($f_{3dB} = 60$ Hz) and an operational amplifier-based (TL074) unity-gain buffer.

The resistive heaters are driven by a pulse-width-modulated signal ($f = 1$ kHz) from the digital board separated by high-impedance unity-gain buffers and BJT/p-MOSFET drivers powered by an on-board single-to-dual-polarity DC/DC converter (12 VDC, Traco Power) or directly from a power supply connector (19 VDC max). Bypass capacitors were used to filter electronic noise. Alternating currents caused by ripple voltages were removed by 0.1 μF and 1 μF tantalum electrolytic capacitors coupled to each integrated circuit on the board. The complete circuit diagram of analog board of the artificial gland controller module is shown in Figure 4.

2.2.2. Chemoreceiver. 2.2.2.1. SAW-based biosensor. SAW resonator devices were chosen as sensor devices due to their high sensitivity, fast response, robustness, small size, and low cost. SAW devices can be employed to detect changes in the electrical (e.g. conductivity and dielectric permittivity) and mechanical (e.g. mass density and viscosity) properties of the adjacent environment by measuring the changes in the propagation characteristics (attenuation and phase) of the SAW travelling along the sensor surface. Since biological cell coatings require the presence of liquid media, for cell-based SAW sensors, it is necessary to use acoustic waves with a single horizontal polarization in the direction normal to the propagation direction lying in the plane of the surface (i.e. a shear wave) for which no longitudinal wave is radiated even if the propagation surface is loaded with liquid [9]. Although several piezoelectric substrates (e.g. $LiTaO_3$ [10], $LiNbO_3$ [11], $La_3Ga_5SiO_{14}$ [12], ZnO [13], and quartz [14]) are suitable for liquid phase sensing, systems $LiTaO_3$-based systems are attractive due to a relatively high electromechanical coupling coefficient [15]. The changes in the velocity, $\Delta v/v$, and the attenuation, $\Delta\alpha/k$, of the propagating SH-SAW due to the response of the sensing layer to ligands can be approximated by the following equations [16]:

$$\frac{\Delta v}{v} = -\frac{K^2}{2}\frac{(\sigma'/\omega)^2 + \varepsilon_0\left(\varepsilon_r' - \varepsilon_r\right)\left(\varepsilon_r'\varepsilon_0 + \varepsilon_P^T\right)}{(\sigma'/\omega)^2 + \left(\varepsilon_r'\varepsilon_0 + \varepsilon_P^T\right)^2} \tag{1}$$

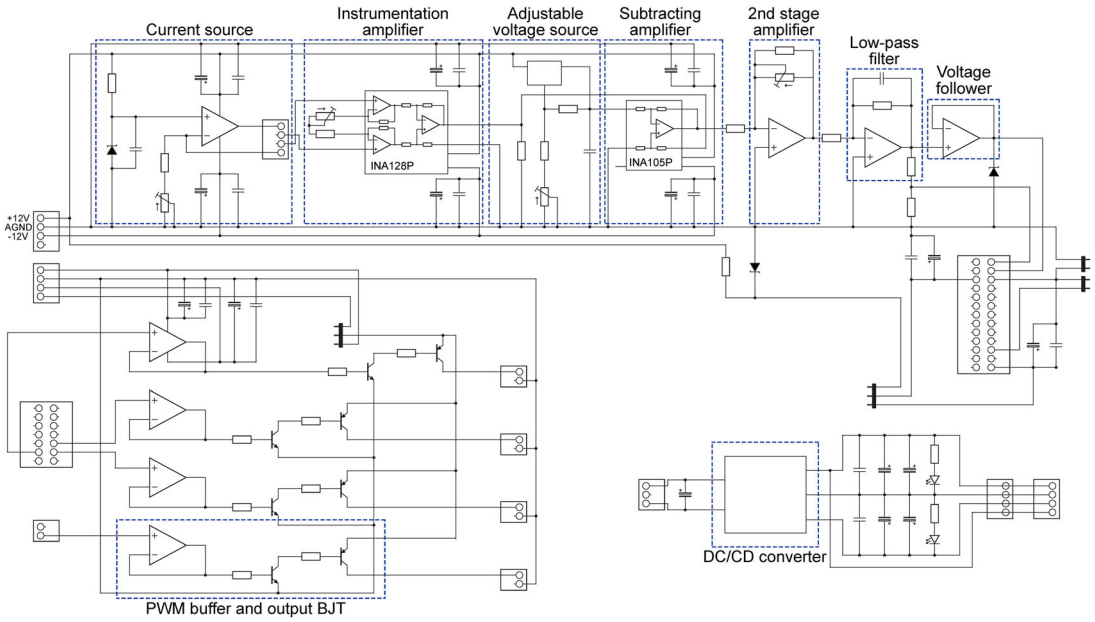

Figure 4. (a) Time-domain evolution of x1(_), y1(_), and (b) evolution of x2(_), y2(_) for a second-order cooperative FRCNN.

DOI: 10.1002/cta

$$\frac{\Delta\alpha}{k} = -\frac{K^2}{2}\frac{(\sigma'/\omega)^2\left(\varepsilon_r\varepsilon_0 + \varepsilon_P^T\right)}{(\sigma'/\omega)^2 + \left(\varepsilon_r'\varepsilon_0 + \varepsilon_P^T\right)^2} \tag{2}$$

Here, k is the wave number, ω is the angular frequency, K^2 is the electromechanical coupling constant, ε_0 is the electrical permittivity of free space, $\varepsilon^T{}_P$ is the effective permittivity of the piezoelectric crystal, ε_r is the relative permittivity of the unperturbed sensing layer, and ε'_r and σ' are the relative permittivity and conductivity of the perturbed sensing layer, respectively.

2.2.2.2. Biological functional layer. Although cell-based sensing can be implemented using a number of cell types (e.g. yeast [17], HEK-293 [18], Sf9 [6]), several characteristics of Sf9 make these the ideal candidate for acoustic sensor applications: Sf9 cells can be deposited on various piezoelectric substrates onto which the cells adhere within ~45 min at the desired confluency eliminating the need for a lengthy and infection-sensitive cell culturing process. The cell line employed as the functional layer for the SAW biosensors is derived from parental colony *Spodoptera frugiperda* (Sf).

The principle of operation of the SAW biosensor is that upon ligand binding, the cells with receptors change their physiological properties, such as mass, stiffness or cytoplasmic Ca^{2+} concentration that, in turn, is detected by the acousto-electric device. The excellent specificity to the target ligands is the direct consequence of the specificity of the transfected ligand binding receptors expressed in the membrane of the Sf9 cells.

The design of the sensors is based on the dual bio-SAW concept [6] where both sides of the dual pair are covered with biological cells; however, only cells on one side are functionalized with specific ORs, while the other side serves as a reference channel. This configuration enables a differential output that is free of non-specific responses, common mode noises, and environmental effects, and ensures that the measured responses are produced purely by the OR-functionalized cells and not by the medium.

Recognition of a broad range of infochemicals requires the synchronous activity of a variety of receptors such that the diversity of biomolecules can be matched. This concept of a high specificity dual SAW sensor design based on the differential measurement of OR-expressing cells versus cells without ORs is shown in Figure 5(A). Cells with target-specific receptors are deposited on the sensing side of the sensor and cells without receptors on the reference side. Due to the identical

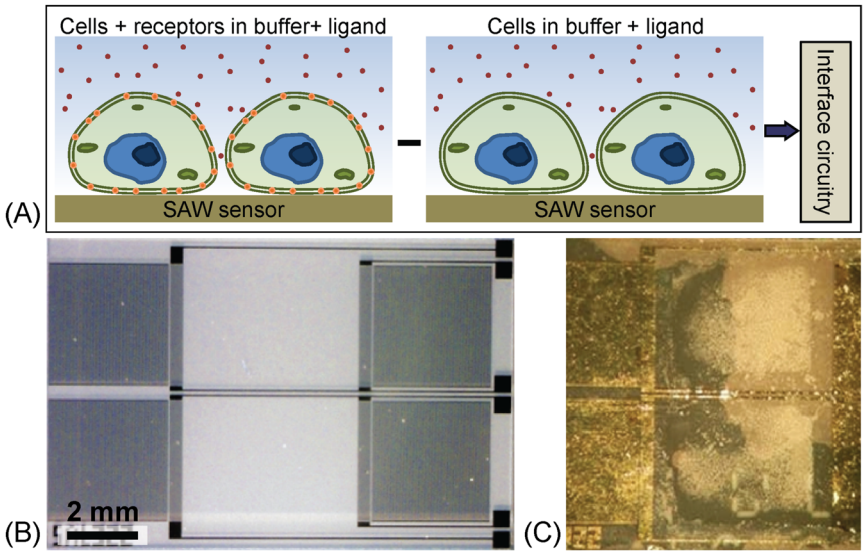

Figure 5. Set Z = Z1 ∪ . . . ∪ Z6 ⊂ bd(K3) of initial conditions for which the solutions of a third-order cooperative FRCNN cannot be prolonged for times $t < 0$ (gray). The figure also displays the trajectory in the time interval [_12.55, 0] s for a solution starting at ^x ¼ 0:54; 0:5; 0:46Þ′ 2 intðK3Þ _ (point ◦) at $t = 0$. The solution is seen to hit the set Z6 (point _) at the instant $t_- = -12.55$ s.

DOI: 10.1002/cta

sensor design, the spatial proximity of the sensing areas, and the similarity of the various cell types, the differential output is free of both non-specific responses and common mode variations. Figure 5 shows a micrograph of a SAW resonator sensor before (B) and after (C) cell depositions. The top side of the sensor was covered with OR-expressing cells while the bottom side with cells without ORs.

We believe that by employing cell coatings that express different ligand-specific ORs on an array of sensors, it is possible to construct a simplified artificial insect antenna.

2.2.2.3. Bi-compartmental model of cell-sensor interaction. A bi-compartmental mathematical model has been developed to describe the cell-based sensor system that can help both understand and estimate the expected frequency response. The basic model is shown in Figure 6 and comprises a set of cells lying on top of a piezoelectric surface. The fractional coverage of the surface by cells is f_c, and so the model is of a compartment of volume fraction f_c of cells and a volume fraction $(1\text{-}f_c)$ of liquid medium. In a first approximation, we assume that the cell volume fraction is a constant, i.e. that the cells do not swell when in different media or when a ligand binds onto the receptors. However, as shown in Figure 6 (inset), when the ligand binds onto the ORx, it is coupled to the co-receptor OR83b with two possible mechanisms proposed in the literature [19]. The coupling could be a slow one via a secondary messenger cAMP or a direct one. The co-receptor opens the calcium ion channel so that the concentration of calcium ions increases inside the cell, thus increasing the overall intracellular ionic conductivity. This mechanism is well known and is confirmed by both calcium imaging techniques and the measurement of the related cell membrane (Nernst) potential.

The frequency response of a SAW resonator depends upon the mass-density, ρ, viscosity, η, electrical conductivity, σ, and dielectric permittivity, ε, of the adjacent medium. Any change in the resonant frequency could be associated with one or more of these variables. Using the differential theorem the total frequency shift Δf can be related to changes in the dependent parameters. In addition, we assume the contributions from the cell and medium are independent (i.e. linearly separable), namely:

$$\begin{aligned}\Delta f = {} & f_c\left\{\frac{\partial f_{cell}}{\partial \rho_{cell}}\Delta\rho_{cell} + \frac{\partial f_{cell}}{\partial \eta_{cell}}\Delta\eta_{cell} + \frac{\partial f_{cell}}{\partial \sigma_{cell}}\Delta\sigma_{cell} + \frac{\partial f_{cell}}{\partial \varepsilon_{cell}}\Delta\varepsilon_{cell}\right\} + \\ & (1-f_c)\left\{\frac{\partial f_{liq}}{\partial \rho_{liq}}\Delta\rho_{liq} + \frac{\partial f_{liq}}{\partial \eta_{liq}}\Delta\eta_{liq} + \frac{\partial f_{liq}}{\partial \sigma_{liq}}\Delta\sigma_{liq} + \frac{\partial f_{liq}}{\partial \varepsilon_{liq}}\Delta\varepsilon_{liq}\right\}\end{aligned} \tag{3}$$

We use here a reference SAW sensor, and so we actually measure the response of the cells with the ligand-specific cells only and do not see any changes in the liquid background. Hence, Equation (3) simplifies to:

$$\Delta f_{ligand} \approx f_c\left\{\frac{\partial f_{cell}}{\partial \rho_{cell}}\Delta\rho_{cell} + \frac{\partial f_{cell}}{\partial \eta_{cell}}\Delta\eta_{cell} + \frac{\partial f_{cell}}{\partial \sigma_{cell}}\Delta\sigma_{cell} + \frac{\partial f_{cell}}{\partial \varepsilon_{cell}}\Delta\varepsilon_{cell}\right\} \tag{4}$$

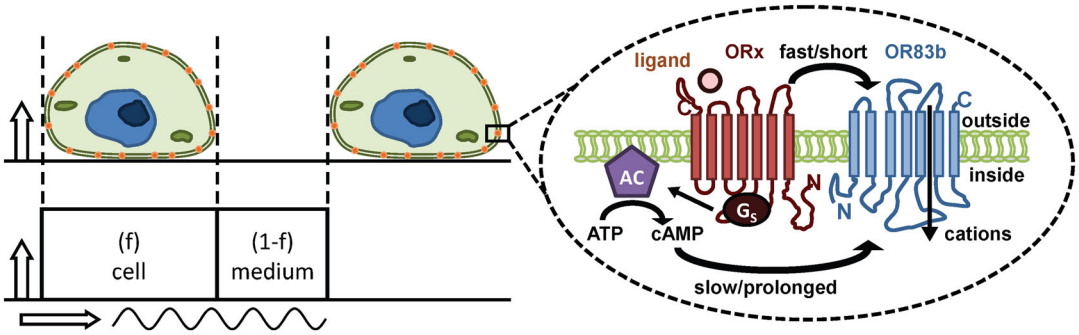

Figure 6. Neuron interconnection graph for a seventh-order FRCNN.

DOI: 10.1002/cta

These four loading terms are associated with the change in the mass of the cell when the ligand binds, the change in viscosity or cell stiffness, the change in cell conductivity, and the change in cell dielectric permittivity.

The addition of small concentrations (10 μM) of the insect sex pheromone 11-cis vaccenyl acetate ($C_{20}H_{38}O_2$), for example, will result in the saturated binding of 310 Dalton molecules to about 100,000 receptor sites per cell with about 10,000 cells per SAW sensor. This is equivalent to about 1 femtogram of mass and is thus below the resolution of our SAW sensor. In contrast, the intracellular calcium concentration will increase by some micromolar value in a background ionic concentration (including sodium and potassium) of 10 millimolar concentration. It is possible to detect a change of one part in ten thousand with a SAW resonator and this should correspond to a frequency shift of a few hundreds of hertz. This is indeed the level of frequency shift observed [6] although we can rule out changes in cell viscosity/stiffness or indeed cell size.

2.2.2.4. SAW sensor drive circuitry. Ligand-induced perturbations of the SAW present themselves as changes in the attenuation and velocity of the wave (see Equations (1) and (2)); however, the real-time monitoring and processing of these characteristics would require complex circuitry not suitable for integrated systems. Measuring the wave velocity changes indirectly by using the SAW sensor as a resonating element gives great measurement precision and requires very simple circuit solutions. A basic configuration required for this is shown in Figure 7(A) where the sensor is placed in the feedback loop of a radio-frequency amplifier.

For the circuit to oscillate, two conditions must be satisfied simultaneously: (1) the total loop gain must be greater than 1 and (2) the phase shift for the entire loop must be 0°. When the phase velocity of the acoustic wave is changed, the phase of the loop also changes, and the phase condition of oscillation is satisfied at a different frequency, thus, the resonant frequency of the circuit is shifted which can be measured with high accuracy using a frequency counter.

The radio-frequency amplifier provides the gain to compensate for the losses that occur in the feedback loop. The total loop loss is the sum of the SAW device's insertion loss (<10 dB typically), the loss due to mass loading of the device during operation (~4 dB), attenuation by the filter, and as a result of imperfect impedance matching (~1–2 dB). For stable operation under a variety of conditions, a gain margin of 3 dB is needed; therefore, the amplifier is required to have a gain of 18–20 dB. Silicon monolithic integrated circuit power amplifiers are an attractive choice for this application as they are low power (3.3–5 V and 10–20 mA), internally matched to 50 Ω, and provide very flat gain over a wide frequency range which makes them suitable for a broad variety of SAW devices. Moreover, they require only a few external components and have layout footprints comparable to passive surface mount components.

To suppress oscillations at spurious frequencies, a low-pass or band-pass filter is included in the feedback loop. The oscillator circuit may also include input and output impedance matching

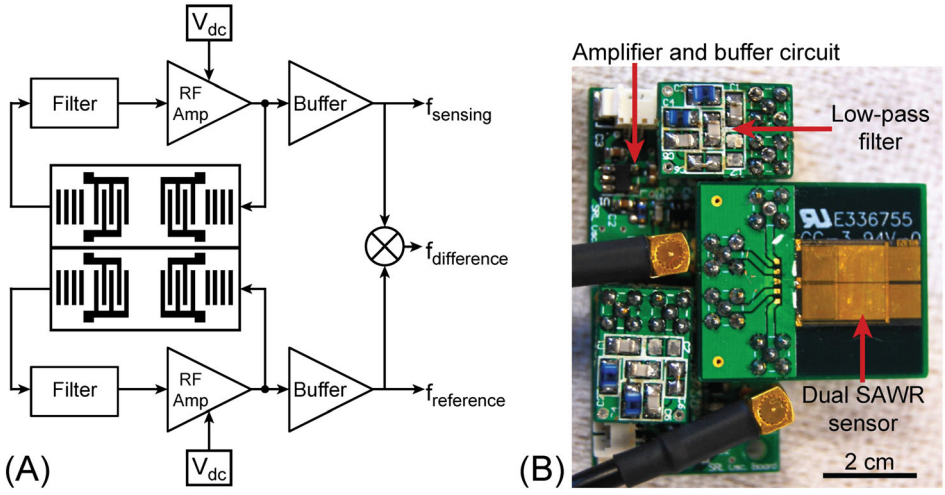

Figure 7. Oscillatory behavior of x1(_) and y1(_) for a seventh-order FRCNN.

DOI: 10.1002/cta

networks for the sensor, a phase shifter, and an attenuation adjustment network. However, in our design these components are unnecessary because the SAW transducers were designed to have 50 Ω both input and output impedances, the components of the low-pass filter were selected to provide phase matching and by using a variable power supply RF amplifier, the loop gain can be adjusted within a wide range.

To enable the use of SAW devices of different resonant frequencies, the oscillator circuit was implemented using three separate printed circuit boards that are connected via high-frequency micro-miniature gold coaxial connectors. The main board contains the active components, the filter board the passive components necessary for filtering and phase matching, and the sensor board the SAW device. The complete discrete-component high-frequency oscillator circuitry driving a 60-MHz metalized dual SAW sensor is shown in Figure 7(B).

Although SAW sensors are highly sensitive, their serious drawback is the relative low selectivity of substrate materials. A common strategy to provide sufficient selectivity to vapor-phase analytes is the application of sensor arrays utilizing low selectivity functional coatings (e.g. polymers [20]) followed by sophisticated data processing and pattern recognition techniques. By employing a functional coating of biological cells expressing specific ligand-receptors, sensor specificity improves significantly to enable molecular recognition.

2.2.3. Biologically constrained neuromorphic network. In order to process SAW receptor signals and relate them to ratio decoding and blend recognition, a biologically constrained computational model mimicking the ratiometric processing in the AL of *Lepidoptera* was developed and implemented. The AL of the insect brain is formed by spherical neuropilar structures called glomeruli that house synaptic contacts between ORs neurons (ORNs) and second-order projection neurons (PNs) that are under inhibitory control from globally connected local interneurons (LNs). PNs which represent the key output of the AL to higher brain centres (in the mushroom body) of the insect are known to encode blend information. In species using sex-pheromone communication, the males have a specialized structure known as the macroglomerular complex (MGC), which consists of some enlarged glomeruli that receive exclusive input from pheromone sensitive ORNs.

Individual neuron dynamics are modelled using a first-order differential equation that describes the evolution of the firing-rate activity over time,

$$\tau \frac{da_i}{dt} = -a_i(t) + \mathrm{S}\left(\sum_{j\in P} w_{i,j}a_j(t) - \sum_{k\in L} w_{i,k}a_k(t) + R_i(t)\right) \tag{5}$$

where a_i is the activation level of the i^{th} interneuron; P is the subset of interneurons that are PNs, and L the subset of interneurons that are LNs; $w_{i,j}$ is the strength of synaptic influence of neuron j on the activity of neuron i (similar for $w_{i,k}$); $R_i = v_{i,1}r_1 + v_{i,2}r_2 = \mathbf{v}_i.\mathbf{r}$ is the afferent input from receptor neurons to the i^{th} interneuron, which is the sum of glomerular inputs from the two ORN types, $\mathbf{r} = (r_1,\ r_2)$, weighted by the strength of connections, $\mathbf{v_i} = (v_{i,1},\ v_{i,2})$; S is a sigmoidal squashing function that limits the neuronal activity to values between 0 and 1 while still allowing a linear-like response to a range of input levels between non-activation and saturation; and τ is the time constant governing the speed of the neuronal dynamics (set at 10 ms for all PNs and at 20 ms for all LNs). Note that synaptic influence from PNs is excitatory and therefore positive, while LNs are inhibitory and negative.

The connectivity of the networks was determined according to known morphological principles of the moth MGC and is shown in Figure 8(A). Two MGC glomeruli are modeled, which are the convergent sites for the axons of two ORN types, one glomerulus for each type accordingly. 30 PNs and 30 LNs were modelled in each network. The receptor neurons provide afferent excitation to both classes of AL interneurons, whereas PNs, in this case being uniglomerular, receive excitation from just one type of receptor. On the other hand, LNs, being multiglomerular, can receive excitation from both receptor types. LNs form random inhibitory connections with PNs. Neurons of the same class can form interconnections only within each shaded region enclosed by dashed lines. Within the blue and green shaded areas, PNs have random excitatory interconnections. In the red shaded area, LNs can either have all-to-all inhibitory connections to produce Winner Takes All

DOI: 10.1002/cta

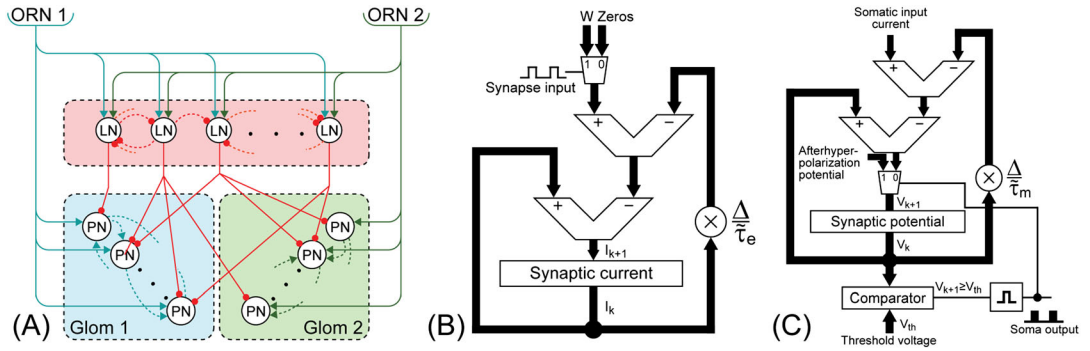

Figure 8. Neuronal connectivity schematic. Connections between neurons of different classes are shown. ORN - Olfactory receptor neuron, LN - Local interneuron, PN - Projection neuron. Solid circles show inhibitory synapse and arrows excitatory synapse connections. The PN population constitutes the main antennal lobe ratiometric processing output (A); Register transfer level description of the exponential decay synapse architecture (B); Register transfer level description of the leaky integrate-and-fire soma architecture (C).

(WTA) networks, or random inhibitory connections (with a connection probability of 0.25) to produce Winnerless Competition (WLC) networks (see below).

In the real-time spiking implementation of the AL model, synaptic dynamics are described by an exponential decay process, convolved over multiple spike inputs occurring at times (t_1, t_2, ... t_j, t_l) to give the total dendritic current as

$$I(t) = w \sum_{j=1}^{l} H(t - t_j) e^{\left(-\frac{t-t_j}{\tau_e}\right)} \tag{6}$$

where $H(\cdot)$ is the Heaviside function, w is the synaptic efficacy (i.e. weight) that determines the current increment in response to the arrival of each presynaptic action potential, and τ_e the time constant of the exponential decay, resulting from the arrival of each presynaptic action potential. The register transfer level (RTL) description of the synapse, which has been directly implemented in programmable logic, is shown in Figure 8(B) [21]. Neurons within the real-time spiking AL model were implemented as leaky integrate-and-fire (LIF) neurons (soma) with exponential decay synapses. The RTL description of the LIF soma shown in Figure 8(C) integrates dendritic currents over time to generate a membrane potential which drives the spiking process [22].

The hardware implementation of the neuromorphic AL model using a field-programmable gate array (FPGA) for real-time chemosensory input processing requires additional elements to control the data flow from stage to stage. The system architecture is shown in Figure 9. A PC is used for sending and receiving information from the AL model (enclosed in the dashed box) in real time and to configure the initial parameters of the circuit (e.g. synaptic weights). Ratiometric identification and classification are carried out by the AL circuit. The AL representation shows the OR neurons 1 and 2 (ORN 1 and ORN 2) depicted as green and yellow triangles, respectively. ORNs are connected toward every LN of the system. ORNs make excitatory synapses with LNs (green and yellow circles); therefore, every local neuron receives input from both receptor neurons. LNs each have a probability to form inhibitory interconnections to other LNs (but this is fixed at runtime), as illustrated by the dark blue circles from the output of the local neurons. Excitatory inputs from the ORNs and inhibitory inputs from LNs converge to an adder which superimposes spike trains from multiple sources to drive the target neuron. The AL model also contains two glomeruli; however, unlike the LNs which receive input from every ORN, each glomerulus only receives input from a particular ORN. Principal neurons can also make excitatory connections towards principal neurons within a single glomerulus, but connection towards another glomerulus is not allowed. On the other hand, LNs can make inhibitory synapse with PNs of any glomerulus. As in the case of LNs, convergent spike trains are superimposed to drive PNs within the model.

Initially, model configuration parameters are stored in the block memory (BRAM) within the FPGA that are then distributed to their corresponding synapse by means of a decoder, which enables a register

DOI: 10.1002/cta

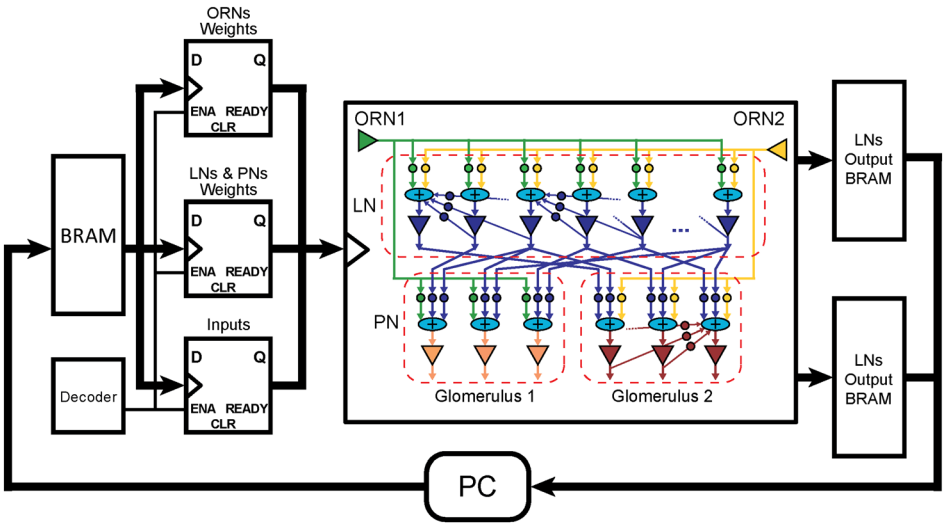

Figure 9. Schematic representation of the real-time implementation of the pheromone model on an FPGA and the flow of information between the PC and the FPGA. The triangles represent integrate-and-fire neurons, and the circles represent both excitatory and inhibitory dynamical synapses.

to store the configuring parameter. Once all parameters are stored in their corresponding register, the neuronal model processes the information, and the outputs are stored into two BRAM memories, one for spiking response from LNs and the other for the outputs of the model, i.e. the spiking response from principal neurons. The output is sent to the PC and stored for offline processing and analysis.

This arrangement of LNs allows more than one glomeruli to respond to one ORN (i.e. sensor) and thus permits the encoding of ratios of different ligands. Classification takes place from the outputs of the PN population. The response of the LN population is displayed in Figure 10(A), showing firing rates (spike densities) that vary over time and between individual LNs. This spatiotemporal response is the result of the joint action of the receptor neurons and the lateral inhibition among LNs. There are cells that show high activity levels (high spike density), whereas other cells are silent throughout. Figure 10 (B) displays the spiking output from the PN population which represents the main output of the AL model. Here, only a few cells show activity resulting in a sparse representation of the sensory (ORN) inputs; in this example, two cells show a dominant role in the system. Other cells also show some spiking activity, but to a lesser extent than the two dominant cells. We call this WTA dynamics that can occur in the model under certain conditions of connectivity (that depends upon symmetry in the model). In other connectivity conditions (symmetry breaking), we observe more temporally complex spatiotemporal dynamics that is reminiscent of WLC.

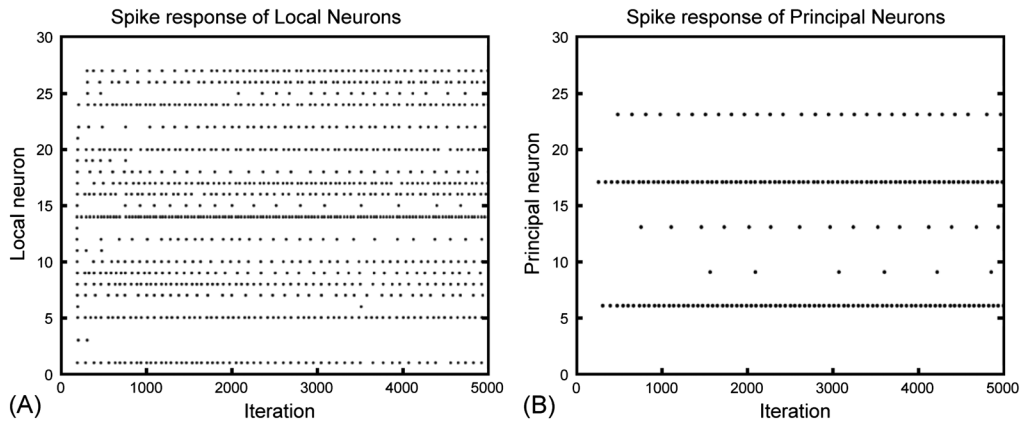

Figure 10. Spike responses from the LN population (A) and the PN population (B).

DOI: 10.1002/cta

The principal neurons are the main output of the AL as is also the case in insects, and so the spike response reflects the response of the AL to a certain stimulus. The model can be controlled by changing the parameters, i.e. the synaptic weights, the time constant of the cells, and the threshold parameter of the neurons.

The full spiking WLC AL model consisting of 2 ORNs, 30 LNs, and 2 glomeruli with 15 PNs each was implemented in an FPGA which enables the verification of the model's behavior in a short time due to its hyper real-time performance (approximately 3 orders of magnitude faster than the biological time it is representing). The corresponding die footprint is shown in Figure 11(A), and an example for the firing rate (spike density) dynamics to a set of synthetic ratio inputs is shown in Figure 11(B).

2.2.4. VLSI implementation. As part of the development of a compact and low-power portable chemoreceiver system, the olfactory sensor drive and control circuitry was deployed in an application-specific integrated circuit (ASIC). The ASIC comprises of an analog front-end module and a digital controller block as shown in the system architecture diagram in Figure 12.

The analog module is capable of supporting up to four dual detection channels and replaces the entire discrete sensor module shown in Figure 7. To facilitate the use of SAW sensors of different device characteristics and varying operating conditions, the circuit employs programmable gain amplifiers, shown in Figure 13(A), which can be set to 20 ± 10 dB using a 3-bit controller. The cutoff frequency of the amplifier was designed to be over 900 MHz to enable the use of ultra high frequency sensors utilizing wireless interrogation at 868 MHz. To achieve this application flexibility and performance with the selected AustiaMicroSystems (AMS) S35 BiCMOS fabrication process, the programmable gain control was implemented using a constant base current bias circuit topology. Temperature instability and the dependence of the bias resistance, R_b, on the ß parameter of the transistors limit the performance of this topology; however, the flexibility provided by the programmable gain control in terms of oscillation adjustment can resolve the latter issue.

The analog oscillator output signals can be measured directly or through a buffer stage, and a balanced mixer, for two of the detection channels, is also included to generate a common mode-free differential output signal. The filter circuits that remove the unwanted overtones are implemented externally due to the relatively large inductance values (~10–150 nH) required for the range of operating frequencies. In addition, a diode-based temperature sensor is used to provide moderate-precision temperature measurement of the chip.

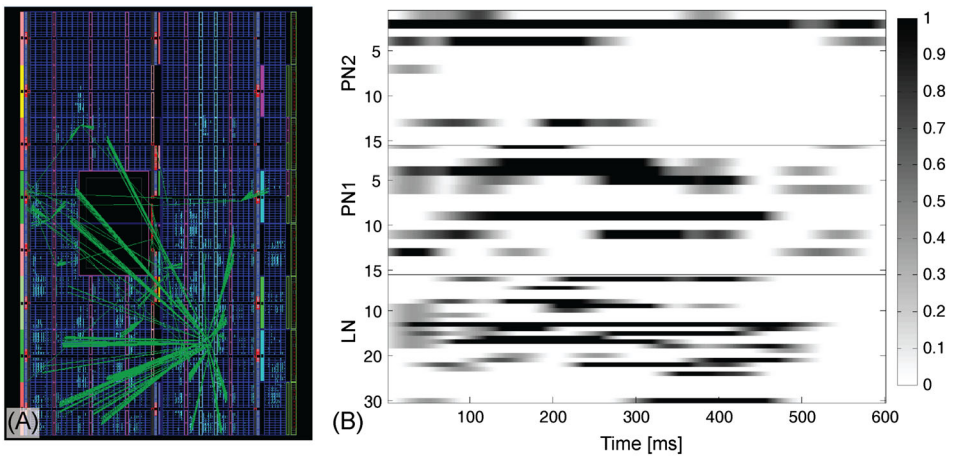

Figure 11. FPGA die footprint of the AL model consisting of 2 ORNS, 30 LNs, and 2 glomeruli with 15 PNs in each glomeruli. The model occupies 3095/11200 logic slices. (A) Example firing rate dynamics over time for the LNs as well as PNs in each glomerulus (LN, PN1, and PN2 populations of the model before learning) showing more temporally complex 'Winnerless Competition' (WLC) dynamics. In this case, the stimulus pulse duration is 500 ms starting from time 0. The neuron firing rate in the figure is normalized by the maximum firing rate frequency (B).

DOI: 10.1002/cta

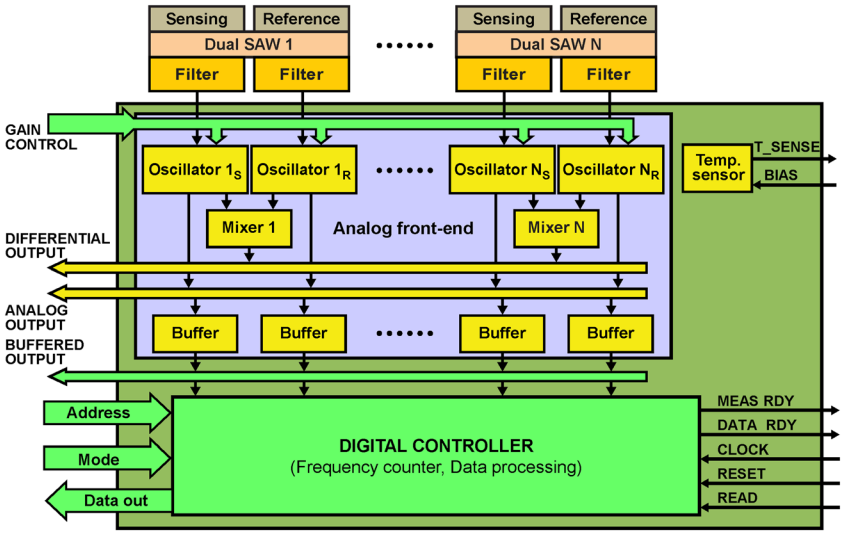

Figure 12. Schematic block diagram showing the system architecture of the integrated chemoreceiver system (excluding FPGA).

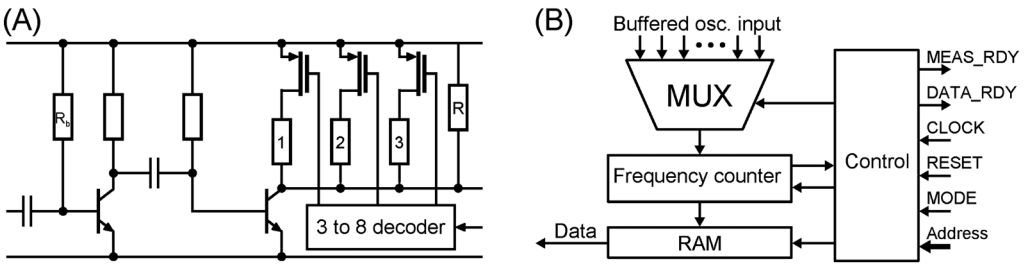

Figure 13. (A) Circuit diagram of the programmable gain wideband amplifier stage of the analog oscillator module. (B) Schematic block diagram of the digital controller module.

The digital controller module, shown in Figure 13(B), performs frequency measurements on all of the eight channels to 32-bit accuracy, computes and stores the difference between the measured and the reference frequency, and allows data reading in 4×8 blocks. The controller is driven by a 10-MHz input clock, and the ASIC is capable of measuring the oscillation frequency of the sensor circuits with 1-Hz resolution. Since only the relative shift in frequency of the detection channels carries valuable information, the digital module also performs frequency mismatch compensation by

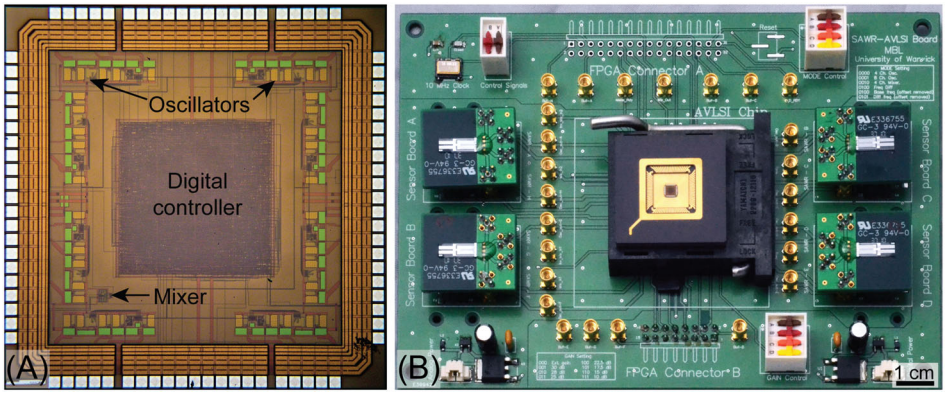

Figure 14. (A) Optical micrograph of ASIC chip showing the main circuit components. (B) Photograph of the hybrid system including printed circuit board, SAW sensors, ASIC chip, and analog and digital outputs.

DOI: 10.1002/cta

digitally measuring and storing the base frequency of each channel and removing the calculated offset. The digital output data format is compatible with the back-end FPGA block that implements the neuromorphic blend specificity model for blend classification.

The ASIC has been developed using a 0.35-μm 3.6-V high-frequency SiGe BiCMOS AMS process and was fabricated at AMS. An optical micrograph of the fabricated 3×3 mm^2 chip is shown in Figure 14(A). A photograph of the printed circuit board including four dual SAW sensors, the packaged ASIC chip and input/output connectors is shown in Figure 14(B).

3. CONCLUSIONS

We have described the design and development of a new class of communication technology that is based on the exchange of chemical information between insects. The infochemical communication system presented here utilizes functional equivalents of the molecular, sub-cellular, and cellular machinery comprising the pathway between pheromone production and detection in an insect. Both chemical signal generation and detection are replicated by taking a systematic and modular approach that implements reaction steps as biosynthetic modules which are then hierarchically integrated as a technological solution. This forms a new branch of information technology employing ratiometrically programmed infochemicals to encode multiple channels of information to communicate over space and time.

The development of an artificial chemoemitter (or gland) comprising a microreactor and a micromachined evaporator for the production and release of infochemical mixtures into the environment has been described. The presented microevaporator module allows precise dosing of chemical compounds that is crucial for ratiometric information encoding. The capability to vary the pheromone flux over a wide range combined with the temporal modulation of the pheromone blend composition creates the potential for increased bandwidth chemical communication channels.

The biological sensing module comprises a dual SAW resonator device coated with a biological functional layer of OR expressing Sf9 insect cells and the associated oscillator circuitry. The sensor design utilizes the dual bio-SAW concept where the differential output of a functionalized and a reference device is measured enabling a response that is free of non-specific responses, common mode noises and environmental effects. This module was used to detect successfully a biomolecular agent (octopamine hydroxide) in the micromolar range. It enables the detection of receptor-specific ligand binding and can be used more generally to monitor cell biochemistry (e.g. ligand binding and intracellular ionic conductivity) and physiology (e.g. cell stiffness/viscosity, viability) [6].

The sensor signals are processed by a neuromorphic model of the AL of the insect embedded within an FPGA. The model comprises 2 ORNs, 30 LNs, and 2 glomeruli with 15 PNs. This relatively small neuronal architecture has the ability to classify pheromone blends and represents the state-of-the-art in insect AL computational neuroscience.

Besides, the measurement of pheromone elicited cellular responses, the communication system design presented here has also been successfully used to demonstrate the concept of infochemical-based ratiometric communication. Using binary mixtures of plant compounds, ethyl acetate, and isoamyl alcohol, information was ratiometrically encoded and released into the environment, then successfully detected and recovered with an array of polymer-coated SAW resonator sensors using steady-state sensor outputs [23]. The chemoreceiver module can facilitate high-resolution real-time measurements as well for dynamic feature extraction and data analysis using a neuromorpic model. An FPGA implementation has been shown to recover ratiometric information from the early transient phase of the sensor response [24].

In conclusion, the combination of precise spatiotemporal signal generation with highly sensitive and selective chemical or biological detection and signal processing provides a powerful tool for small-scale, yet high-throughput infochemical communication. Moreover, this novel integrated infochemical communication system can serve as the foundation for a new form of information transmission which can be implemented in VLSI technology. As a low-cost, low-power system, it has potential influence on future developments of automatic identification and data capturing, product labeling, medical diagnosis, and environmental control and monitoring. Further work is being undertaken to integrate the sensors, resonator circuit, and FPGA into a single VLSI implementation.

DOI: 10.1002/cta

ACKNOWLEDGEMENT

This work was funded by the EU as part of a STREP project no. FP6-032275 called 'Biosynthetic Infochemical Communication'.

REFERENCES

1. von Frisch KR, The Dance Language and Orientation of Bees. Oxford University Press London: United Kingdom, 1967.
2. Martínez T, Fabriàs G, Camps F. Sex-pheromone biosynthetic-pathway in spodoptera-littoralis and its activation by a neurohormone. *Journal of Biological Chemistry* 1990; **265**:1381–1387.
3. Sadek MM, Hansson BS, Rospars JP, Anton S. Glomerular representation of plant volatiles and sex pheromone components in the antennal lobe of the female Spodoptera littoralis. *Journal of Experimental Biology* 2002; **205**:1363–76.
4. Cole M, Gardner JW, Rácz Z, Pathak S, Guerrero A, Muñoz L, Carot G, Pearce TC, Challiss RAJ, Markovic D, Hansson BS, Olsson S, Kübler L, Gardeniers JGE, Dimov N, Bula W. Biomimetic insect infochemical communication system. *The 8th Annual IEEE Conference on Sensors* October 25–28, 2009, Christchurch, New Zealand. DOI: 10.1109/ICSENS.2009.5398416
5. Rácz Z, Olsson SB, Gardner JW, Pearce TC, Hansson BS, Cole M. Challenges of biomimetic infochemical communication. *Procedia Computer Science* 2011; **7**:106–109. DOI: 10.1016/j.procs.2011.12.032
6. Rácz Z, Cole M, Gardner JW, Pathak S, Jordan MD, Challiss RAJ. Cell-based surface acoustic wave resonant microsensor for biomolecular agent detection. *The 16th International Conference on Solid-State Sensors, Actuators and Microsystems* June 5–9, 2011, Beijing, China. DOI: 10.1109/TRANSDUCERS.2011.5969348
7. Dimov N, Muñoz L, Carot-Sans G, Verhoeven MLPM, Bula WP, Kocer G, Guerrero A, Gardeniers JGE, Pheromone synthesis in a biomicroreactor coated with anti-adsorption polyelectrolyte multilayer. *Biomicrofluidics* 2011; **5**:034102. DOI: 10.1063/1.3608138
8. Bula W, Dimov N, Muñoz L, Guerrero A, Gardeniers JGE. Artificial gland for precise release of semiochemicals for chemical communication. *The 14th International Conference on Miniaturized Systems for Chemistry and Life Sciences* October 3–7, 2010, Groningen, The Netherlands.
9. Kondoh J, Shiokawa S. A liquid sensor based on a shear horizontal saw device. *Electronics and Communications in Japan (Part 2)* 1993; **76**:69–82. DOI: 10.1002/ecjb.4420760208
10. Kondoh J, Shiokawa S. Liquid-phase microsensor based on surface acoustic wave devices. *Electronics and Communications in Japan (Part 2)* 1998; **81**:9–17. DOI: 10.1002/(SICI)1520-6432(199811)81:11 < 9::AID-ECJB2 > 3.0.CO;2-U
11. Liu D, Clinical analysis of urea in human blood by coupling a surface acoustic wave sensor with urease extracted from pumpkin seeds. *Analytica Chimica Acta* 1995; **307**:61–69. DOI: 10.1016/0003-2670(95)00046-3
12. Berkenpas E, Bitla S, Millard P. Pereira da Cunha M, Pure shear horizontal SAW biosensor on langasite. *IEEE Transactions on Ultrasonics, Ferroelectrics, and Frequency Control* 2004; **51**:1404–1411. DOI: 10.1109/TUFFC.2004.1367479
13. Qiu X, Tang R, Chen SJ, Zhang H, Pang W, Yu H. pH measurements with ZnO based surface acoustic wave resonator. *Electrochemistry Communications* 2011; **13**:488–490. DOI: 10.1016/j.elecom.2011.02.028
14. Baer RL, Flory CA, Tom-Moy M, Solomon D. STW chemical sensors. *IEEE Ultrasonics Symposium* 1992; 293–298. DOI: 10.1109/ULTSYM.1992.275993
15. Kogai T, Yatsuda H, Shiokawa S. Dip-type liquid-phase sensor using SH-SAW. *IEEE Ultrasonics Symposium* 2007; 2091–2094. DOI: 10.1109/ULTSYM.2007.526
16. Kondoh J, Shiokawa S. Shear surface acoustic wave liquid sensor based on acoustoelectric interaction. *Electronics and Communications in Japan (Part 2)* 1995; **78**:101–112. DOI: 10.1002/ecjb.4420780111
17. Hahn T, Tag K, Riedel K, Uhlig S, Baronian K, Gellissen G, Kunze G. A novel estrogen sensor based on recombinant Arxula adeninivorans cells. *Biosensors and Bioelectronics* 2006; **21**:2078–85. DOI: 10.1016/j.bios.2005.10.019
18. Lee SH, Jeong SH, Jun SB, Kim SJ, Park TH. Enhancement of cellular olfactory signal by electrical stimulation. *Electrophoresis* 2009; **30**:3283–88. DOI: 10.1002/elps.200900124
19. Nakagawa T, Vosshall LB. Controversy and consensus: noncanonical signalling mechanisms in the insect olfactory system. *Current Opinion in Neurobiology* 2009; **19**:284–292. DOI: 10.1016/j.conb.2009.07.015
20. Penza M, Cassano G, Sergi A, Lo Sterzo C, Russo MV, SAW chemical sensing using poly-ynes and organometallic polymer films. *Sensors and Actuators B: Chemical* 2001; **81**:88–98. DOI: 10.1016/S0925-4005(01)00937-6
21. Guerrero-Rivera R, Pearce TC. Attractor-based pattern classification in a spiking FPGA implementation of the olfactory bulb. *Proceedings of the 3rd International IEEE EMBS Conference on Neural Engineering* 2007, Hawaii, USA. DOI: 10.1109/CNE.2007.369742
22. Guerrero-Rivera R, Morrison A, Diesmann M, Pearce TC, Programmable logic construction kits for hyper-real-time neuronal modeling. *Neural Computation* 2006; **18** : 2651–79, DOI: 10.1162/neco.2006.18.11.2651.
23. Rácz Z, Gardner JW, Cole M, Jian Y. Volatile-based Ratiometric Infochemical Communication System Using Polymer-coated Piezoelectric Sensor Arrays. *The 10th Annual IEEE Conference on Sensors* October 28–31, 2011, Limerick, Ireland. DOI: 10.1109/ICSENS.2011.6127377
24. Karout S, Rácz Z, Capurro A, Cole M, Gardner JW, Pearce TC. Ratiometric chemical blend processin\g with a neuromorphic model of the insect macroglomerular complex. *Proceedings of the 14th International Symposium on Olfaction and Electronic Nose* 2011; **1362**:77–78. DOI: 10.1063/1.3626312